# Soft Matter

Volume 1 | Number 1 | Jan 2013 | Pages 1–100

## Soft Matter

www.rsc.org/softmatter

www.rsc.org/softmatter

# Soft Matter

Dynamic Article Links ▶

**ARTICLE TYPE**

# Morphology of Lipid-Like Structured Weak Polyelectrolyte Poly(ethylene oxide)-*block*-Poly(methyl methacrylate) Diblock Copolymers Induced by Confinements

**Dan Mu\*[a], Jian-Quan Li\*[b] and Sheng-Yu Feng\*[c]**

Combined with quantum calculation and mesoscale simulation, the self-assembly of the twelve lipid-structured PEO-*b*-PMMA copolymers (BCPs) with six types of molecular topologies was investigated. The BCPs with MMA species as the connecting center of the other arms present ample mesoscale
10 structures, such as micelles and lamellar or curved lamellar phases, and even macrophase separation occurs for the long-chained BCPs. The excluded volume effect of confinements helps form the vesicle-like structure, which proved to be a possible method of confinement to regulate the phase morphologies or segments distribution and, ultimately, the properties of materials. An analysis of the phase formation process of the short-chained BCP with two hydrophilic EO segments and one hydrophobic MMA
15 segment indicated that four stages were found in both neutral and non-neutral wall confinement, all of which present the hexagonal columnar phase. Surprisingly, when the repulsion effect of the wall to EO segment is greater than that of the MMA segment, such BCP self assembles into crossed columnar phase, and the intersection angle of the orientation of these two sets of cylinder arrays is 75 degrees, which can be used to produce the heterogeneous nanotube arrays. For the short-chained BCP with four arms joined
20 at MMA species and EO segments in the outer region, we found a novel method of exchanging the repulsive preference of wall to EO or MMA species that can control the adsorption or desorption of the lamellar phase with the interval of EO or MMA segments.

## Introduction

Block copolymers (BCPs), are an exciting class of materials in
25 terms of both intellectual simulation and practical utility. The self assembled morphologies of BCPs have found many applications in soft nano-technology and drug delivery and have even served as templates for fabricating advanced materials [1]. The BCPs containing both hydrophobic and hydrophilic blocks gained much
30 attention from the biomedical point of view. All biopolymers are polyelectrolytes, which contain ionizable groups on monomers. The existence of both short-range (excluded volume) and the long-range (electrostatic) interactions causes the behaviors of polyelectrolytes to be different from those of neutral polymers [2-
35 5]. Experimental studies have indicated that a large number of flexible polyelectrolytes have the ability to form various aggregates of three-dimensional networks via covalent cross linking, such as spherical [6] or cylindrical micelles [7-8].

Due to the existence of a hydroxyl group in the last monomer, the
40 tail of the poly(ethylene oxide) (PEO) segment is cationic, whereas the other monomers, being made of one oxygen atom in the ester group and hydrocarbon groups, are anionic. For the poly(methyl methacrylate) (PMMA) segment, carbonyl groups exist both in the tail and in the other parts, with the only
45 difference being the number of hydrogen atoms inducing the former to be cationic and the latter to be anionic; however, their electrostatics are so weak that the electrostatics of these parts can be neglected. Therefore, the PEO-*b*-PMMA BCP, a type of weak polyelectrolyte molecule, can be hypothesized to form certain
50 phase morphologies. In addition, the semicrystalline nature of PEO and the similar solubility parameters of both PEO and PMMA make the study of the relevant phase morphologies a challenging endeavor.

Extensive theoretical and computational investigations on
55 polyelectrolytes have been performed for decades [9-17] to validate the validation of the behaviors of polymer from micro- to macroscale. Because molecular simulation is not an economic or efficient method to study a mass system, the mesoscopic dynamic simulation emerged, which forms a bridge between fast
60 molecular kinetics and slow thermodynamic relaxation and enables investigation of the mesoscale properties of polymeric systems. MesoDyn theory, based on dynamic mean-field theory, is a promising and effective approach to explore the self-assembly behavior of polymers at the mesoscale level. This
65 theory was developed by Fraaije [18-19] and utilizes the Langevin equations to describe the phase separation dynamics and ordering processes of polymeric systems. The striking feature of this method is that there is no priori assumption and artificial assumption [20], and a thorough study of the kinetics of phase

formation can be fulfilled to acquire mesoscopic results that are difficult to obtain via experimental methods.
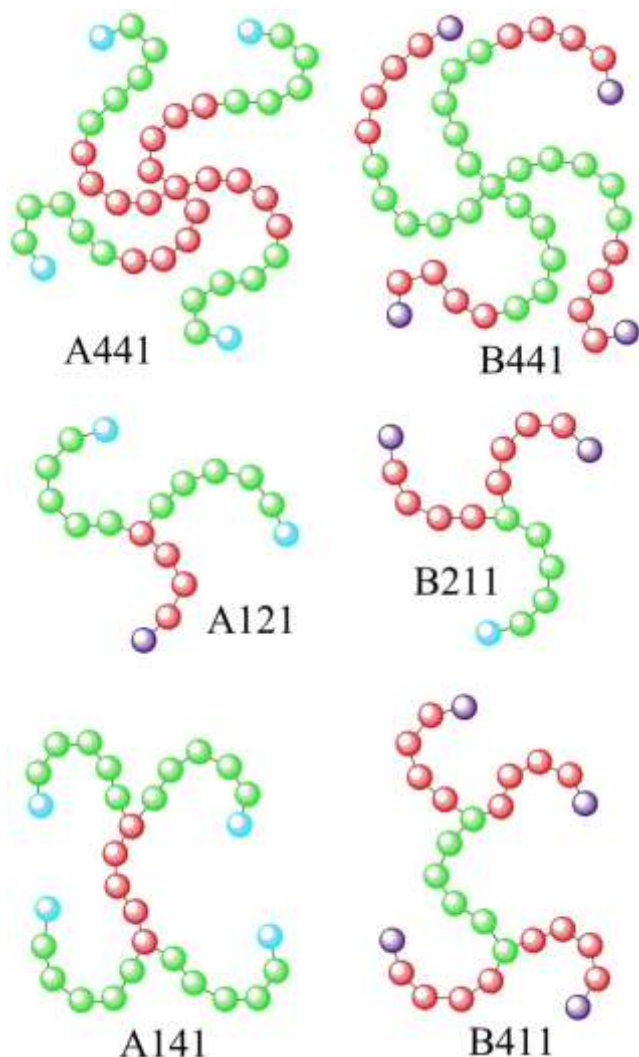


**Fig. 1**. Schematic representation of the PEO-*b*-PMMA BCPs with short
5 chains. The red particles representing the EO blocks are denoted as A, and A' is the terminal of A segments colored in purple; the green particles of the MMA blocks are denoted as B, and B' is the terminal of the B segments colored in cyan.

Different from the bulk phase, the meso-phase of BCP in the
10 confined space can generate novel meso-structures and exhibit more diversity. A large number of studies exist regarding the phase separation of BCPs under one-dimensional (1D) confinement, based on experiments [21], theory [22], and simulations [23-24]. Subsequently, efforts have shifted to two-
15 dimensional (2D) [25-26] and three-dimensional (3D) [27-28] confinements.

In our previous study [29], a wide range of blending ratio composites of PEO and PMMA were investigated at the atomic level, and the corresponding Flory-Huggins parameters, $\chi$, were
20 also obtained. We utilized the MesoDyn package in Material Studio 4.4 software to prove the lower critical solution temperature (LCST) behavior of PEO-*b*-PMMA BCP at high temperature, 400 K, and successfully clarified the conflicting conclusions drawn from different techniques or laboratories.

25 Building on the results of the previous study, in the present study, we extend the research focus to determine the self-assembly and novel phase morphologies of the lipid-structured polyelectrolytes under the 2D (an introduction of walls) and 3D (nanoparticles doping effect) confinements. In addition, a secondary motivation
30 of the present study is to provide a clear analysis of the phase forming mechanism.

## Models and Parameter Settings

An one-to-one relation between the external potential fields and the density fields for each bead type make up the Gaussian chain
35 density functionals. Additionally, the intrinsic chemical potentials ($\mu$) are functionals of the external potentials and the density fields. The coupled Langevin equations constitute a relation between the time derivatives and the intrinsic chemical potentials. Besides, the noise source is associated with the exchange kinetic coefficients.
40 A closed set can be formed by these equations, which can be integrated efficiently on a cubic mesh by a Crank-Nicholson [30] scheme for iteration of the inner loop. In this case, all segments have the same size, and the chain topology depends on the definition of coarsening; in addition, loss of the molecular
45 topology of the original skeleton chains is not recommended.

First, we calculated the solubility parameters of various chain lengths of both PEO and PMMA homopolymers by Molecular Dynamic methods. It was found that when the chain lengths were more than 50 (included), the solubility parameter values would
50 just change in a reasonable range compared with their experimental values. So the representative chain lengths of 50 for both PEO and PMMA chains can be considered as the representative bulk chain lengths. After being divided by the characteristic ratio, two Gaussian chains of $A_5$ and $B_6$ (A denotes
55 EO bead and B denotes MMA bead) were generated to represent the atomistic chains of polymer $PEO_{50}$ and $PMMA_{50}$, respectively [29]. We set $A_5B_6$ as a minimum unit of BCPs. In an attempt to mimic lipid-like structures, a molecular designing strategy was developed using $A_5$ and $B_6$ as the basic and short arms involved.
60 The lipid-like molecular topologies are illustrated in Fig. 1. To distinguish the difference in the electrostatics among the models, we set "A" to be the EO segments, i.e., "A'" denotes the terminal "A" bead with hydroxyl group, whereas "B" represents the repeat monomers of MMA, i.e., "B'" is the terminal "B" bead. The
65 scheme of naming these BCPs is as follows: the first letters "A" or "B" denote the bead type of the branched point, the first and second two numbers present the ratio of EO to MMA segments, and the last number refers to the chain length via a simple notation of the multiple number of each arm based on the $A_5$ or
70 $B_6$. In addition, because it is also significant to investigate the phase morphologies of long-chained BCPs, we enlarged the segment lengths of the six BCPs one time. Taking as a long-chained example B412 to explain this name scheme: each branched point of the MMA segment consists of two arms made
75 of EO segments, which are both connected onto a "B" bead; the ratio of EO and MMA segment is "4:1", and each EO and MMA segment is twice long in chain length compared with the basic $A_5$ and $B_6$ segment, respectively, which is denoted as the last number "2". Detailed molecular information of twelve BCPs of six short
80 chains and six long chains models is listed in Table 1.

**Table 1** Molecular information of the BCPs.

| Model | Arm number in each branch point | Ratio of EO to MMA segments | Chain length[*] | Molecular structure |
|-------|------|------|------|------|
| A441 | 4 | 1:1 | 1 | $A(A_4B_5B')_4$ |
| A121 | 3 | 1:2 | 1 | $A'A_4(B_5B')_2$ |
| A141 | 2 | 1:4 | 1 | $(B'B_5)_2A_5(B_5B')_2$ |
| B441 | 4 | 1:1 | 1 | $B(B_5A_4A')_4$ |
| B211 | 3 | 2:1 | 1 | $B'B_5(A_4A')_2$ |
| B411 | 2 | 4:1 | 1 | $(A'A_4)_2B_6(A_4A')_2$ |
| A442 | 4 | 1:1 | 2 | $A(A_9B_{11}B')_4$ |
| A122 | 3 | 1:2 | 2 | $A'A_9(B_{11}B')_2$ |
| A142 | 2 | 1:4 | 2 | $(B'B_{11})_2A_{10}(B_{11}B')_2$ |
| B442 | 4 | 1:1 | 2 | $B(B_{11}A_9A')_4$ |
| B212 | 3 | 2:1 | 2 | $B'B_{11}(A_9A')_2$ |
| B412 | 2 | 4:1 | 2 | $(A'A_9)_2B_{12}(A_9A')_2$ |

[*] Describes the multiple number of chain length based on $A_5$ and $B_6$.
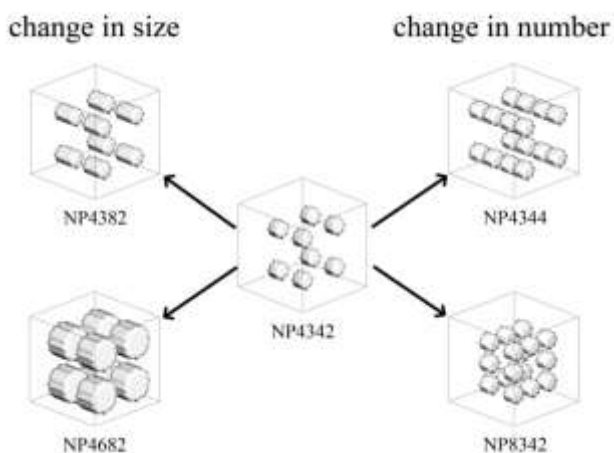


**Fig. 2**. The schematic of NP arrangements.
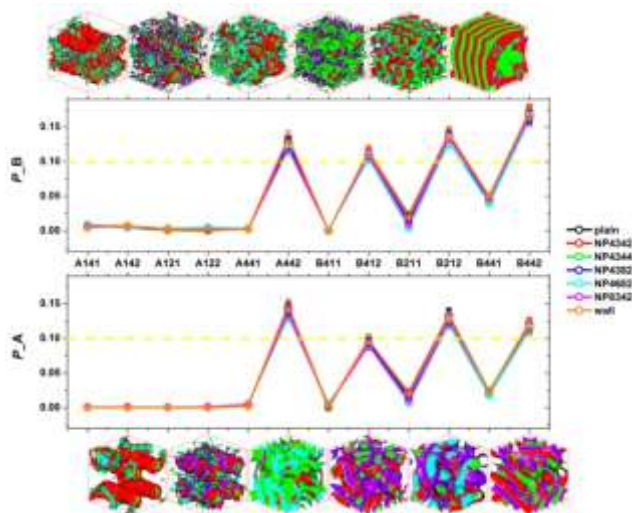


**Fig. 3**. The values of *P* of twelve PEO-*b*-PMMA BCPs induced by various NPs and wall confinements. The reference line colored in yellow is at 0.10. The mesoscale structures of short-chained BCPs induced by NP4344 are listed on the top, whereas the long-chained BCPs induced by NP4344 are listed at the bottom.

Second, the pair-wise interactions of various types of beads are defined by the Flory-Huggins interaction parameters, $\chi$. The pair-wise interaction can be converted into the interaction parameters $\varepsilon_{AB}$, via multiplication of the $\chi$ values with $RT$, where $R$ is the molar gas constant and $T$ is the temperature; the values of $\varepsilon_{AB}$, which are in units of $\varepsilon_{AB}$ is kJ • mol$^{-1}$, are used in the MesoDyn simulation. The $\varepsilon_{AB}$ values in a range of ratios between EO and MMA are listed in Table 2. A positive $\varepsilon_{AB}$ value corresponds to a repulsive interaction between the components A and B, which favors microphase separation or even phase separation. Here, the local gradients of chemical potentials provide the driving force for diffusion, and a set of functional Langevin equations is applied to describe the dynamics of the component densities.

**Table 2** The $\varepsilon_{AB}$ data converted from the $\chi$ values via molecular dynamic[20] calculations at 400 K.

| Ratio of A to B segment | $\varepsilon_{AB}$ |
|-------|------|
| 1:1 | 3.61 |
| 1:2 | 1.14 |
| 1:4 | 0.24 |
| 2:1 | 4.68 |
| 4:1 | 6.23 |

Finally, in addition to the Flory-Huggins parameters, we also introduced the Donnan effect [5] into the polyelectrolytes to describe the electrostatic interactions between beads and to further study the phase behavior. Because only the electrostatic properties involved are considered, the volume of the ions is ignored, which is much smaller than that of the bead species in the system. The interactions between the charged beads are expressed by $\chi_{AB}^D$ in salt strength, where the salt strength of the fluid mediates the electrostatic interactions. In a zero-order approximation, $\chi_{AB}^D = \frac{z_A z_B}{C}$, where *A* and *B* represent the A and B beads, respectively, and $C = 2vc_s$ is the number of ions in the ion bath per unit of bead volume. The zero-order approximation is sufficient for most applications [31-32], including our simulated systems.

We employed cylindrically shaped small objects to mimic nanoparticles (NP) due to the higher number of optional parameters compared to the spherical NPs. In order to investigate the inducing effect of the fix confinement on changing the phase morphologies of BCPs, so the role of the neutral NPs here was just the obstacles, but also with the interaction energy of 5 kJ • mol$^{-1}$ with both A and B beads. Subsequently, five types of nanoparticle arrangements shown in Fig. 2 were designed of different radius, height and number to study their inducing effect on phase morphologies; the results are listed in Table 3. The NP4342 arrangement is the initial arrangement, based on which other NP arrangements were developed. Consider NP4342 as an example to illustrate the naming rule of NP arrangement: there are four NPs in each layer in the YZ plane ($N_P$); the radius ($r_p$) and height ($h_p$) of each NP is 3 nm and 4 nm, respectively; the number of layers along the X axis is two ($N_L$); a total of eight NPs are in the NP4342 arrangement ($N_{tp}$). Beginning with B4342, when the number of layers is doubled to be four, NP4344 is generated; doubling the height of each NP, NP4382 is produced; doubling both the radius and the height of each NP, NP4682 is generated; increasing the number of NPs in each layer yields NP4682. For the 2D confinement of the wall, two slabs are placed both at the top and the bottom of each model.

**Table 3** Five types of nanoparticle arrangements.

| Symbol | $N_P$ | $r_p$ (nm) | $h_p$ (nm) | $N_L$ | $N_{tp}$ |
|--------|-------|------------|------------|-------|----------|
| NP4342 | 4 | 3 | 4 | 2 | 8 |
| NP4344 | 4 | 3 | 4 | 4 | 16 |
| NP4382 | 4 | 3 | 8 | 2 | 8 |
| NP4682 | 4 | 6 | 8 | 2 | 8 |
| NP8342 | 8 | 3 | 4 | 2 | 16 |

All of the simulations in this work were performed in a periodical cubic cell of the size of $32 \times 32 \times 32$ nm$^3$. The grid parameter used was $d = a \cdot h^{-1} = 1.1543$, where $a$ represents bond length, and $h$ is the mesh size. To ensure a stable numerical algorithm and for simplicity, all beads diffusion coefficients were set to be $1.0 \times 10^{-7}$ cm$^2 \cdot$ s$^{-1}$. For numerical speed and stability, the constant noise-scaling parameter of 100 was chosen, and the compressibility parameter was fixed at 10.0. The total simulation dimensionless time was 50,000 steps for each simulation, i.e., 2.5 ms, with the time step $\triangle t = 50$ ns [33]. So the dimensionless time step of 0.5 was applied in the MesoDyn simulation engine, whose definition is the production of the time step being multiplied by the bead diffusion coefficient, then divided by the square of the grid spacing. The ambient temperature was set as 400 K, which has been proven to correspond to the positive $\chi$ values of PEO/PMMA blends in a wide range of compositions. The salt strength $C = 0.01$ mol $\cdot$ L$^{-1}$. We performed *ab initio* calculations using Gaussian 03 suite of programs with the RM062X functional and a 6-311++G(d,p) basis set on PEO and PMMA homopolymers, whose frequency information was in good agreement with the experimental data. Converting the calculated Mulliken charges onto coarse-grained beads, -0.21, 0.42, -0.03 and 0.06 were distributed to each A, A', B and B' bead, respectively.

## Results and Discussion

The order parameter, $P_i$, is an index of the phase separation dynamics over time, defined as the volume average of the difference between the local density squared and the overall density squared, as follows:

$$P_i = \frac{1}{V} \int [\eta_i^2 (r) - \eta_i^2] dr \, ,$$

where $\eta_i$ is a dimensionless density in volume fraction for species $i$. The order parameter should asymptotically approach a stable value as the system achieves dynamic equilibrium. As an assessment index of the degree of phase separation, a large value indicates strong phase segregation; conversely, a very small value indicates a mixed state. Alternatively, the free energy density [34-35] can also be an auxiliary index to judge the thermodynamic state. Because the free energy density is calculated based on dynamic mean-field density functional theory, the free energy density is not routinely calculated for real systems; hence, it is not possible to make a direct comparison with the experimental free energy data [36].

### Aggregation structures of the twelve designed BCPs

Combined with the $P$ values and the corresponding mesoscale structures under NP4344 confinements, as shown in Fig. 3, the phase morphologies are disordered (A141), disordered (A142), disordered (A121), disordered (A122), disordered (A441), curved lamellar (A442), disordered (B411), micelles (B412), micelles (B211), micelles (B212), lamellar (B441) and curved lamellar (B442). The analysis was elaborated as follows:

(1) In general, both of the $P$ values of the A and B beads of long-chained BCPs are higher than those of the corresponding short-chained ones. Because of the long segments and beads composed of EO and MMA in long-chained BCPs, additional movement freedom of translation, rotation and torsion for various portions of the chains exists. This additional movement freedom enables adjustment of the orientation and conformation of the chains, thereby producing more opportunities to assemble with the same segments, leading to the formation of microphases or even phase separation. In addition, more beads in the long-chained BCPs lead to high enthalpy; the formation of aggregates results in the loss of entropy. The synergistic effect of both enthalpy and entropy change with time for long-chained BCPs accelerates the formation of microphase separation. For A442, B412, B212 and B442, the presence of long-chained BCPs with $P$ values all above 0.1 indicates that macrophase separation occurred.

(2) The similarity of the phase morphologies of both A442 and B442 is due to their molecular topology. Both EO and MMA for A442 and B442 have four segments in common, which are most similar to those of other BCPs. However, the positions of the EO and MMA segments are opposite, i.e., the four EO segments are located inside and with A bead as the center joint point, whereas the MMA segments join to the tails of the EO segments and are located outside, resulting in the A442-type molecular topology. On the contrary, switching the positions of the EO and MMA segments, the B bead becomes the center joint point, resulting in the B442-type molecular topology. Therefore, the outmost composition is MMA, with B' acting as the tails for A442; conversely, the outmost composition is EO, with A' acting as the tails for B442. This process explains the conjugated phase morphologies of A442 and B442, for which most MMA segments are distributed outside for the former BCP, whereas most EO segments are distributed outside for the latter BCP. For B441, with the same type of molecular topology as B442, their mesoscale structures are both lamellar, but the aggregate size is small, presented as a narrow distribution of slabs, due to the short-chained structure.

(3) Both B211 and B212 exhibit the same type of molecular topology, with one hydrophobic and two hydrophilic tails, whose mesoscale structures are both micelle-type. Because the long chains of all the arms for B212 BCP provide flexible regulation of the orientation and freedom of motion, the formation of aggregates with the same segments assembled together is likely, and an even macrophase separation can develop. For the short-chained B211, the generated segments should be smaller than the forms for B212; thus, the mesoscale structure is orderly, but the size of the aggregates is small.

(4) The molecular topologies of both B411 and B412 are the same, i.e., a combination of B211 or B212 with the tails of MMA segments. Therefore, the mesoscale structures of B411 and B412 should be similar to those of B211 and B212, which are in a micelle phase. The micelle sizes of B412 are smaller than those of B212, due to the combination of two B212 structures, which can introduce some restrictions to translation, rotation and torsion. As a result, the $P$ value of B412 is slightly smaller than that of B212. Due to the similarity of the molecular topologies of B411 and B412, the mesoscale structure of B411 should be the same as or similar to that of B412; surprisingly, B412 exhibits a

disordered phase and not a micellar phase. In addition, we found 19 small segments with a volume of 55.6 nm³, whose size is quite small, together with a small number of segments that cannot be recognized as microphase separation. Therefore, the *P* value of

5 B411 is much smaller than that of B412.

(5) Compared to A442, the situation of A441 is more similar to that of B411 versus B412; we found 23 small aggregates with a volume of 58.1 nm³ dispersed randomly in the system, and no ordered mesoscale structure formed. Thus, the *P* value of A441 is

10 much smaller than that of A442.

(6) All the phase morphologies of A141, A142, A121 and A122 are disordered, with few small aggregates of volume in the range 20 to 30 nm³ in the system, resulting in the low *P* values. Although the molecular topologies of these four molecules are

15 the result of converting both the EO and MMA segments of B411, B412, B211 and B212, the phase morphologies are absolutely different. There are two hydrophobic arms and one hydrophilic arm in lipid-like structured A121 and A122 with the same molecular topology, whereas the A141 and A142 are a

20 combination of two A121 and A122, respectively, with the two terminals of the EO segments joined together. The molecular structure and reduced number of EO segments inhibit the formation of the segments; furthermore, the mesoscale structure is disordered.

25 From the discussion in this section, we found a BCP with the B bead as the center branching point, tends to form an ordered phase morphologies, especially for long-chained BCPs. On the contrary, for a BCP with A bead as the center branching point, the formation of segments, let alone phase separation at

30 mesoscale, is inhibited, especially for the BCPs with fewer hydrophilic segments.

To determine the degree of influence on changing the phase morphologies, we defined a new parameter to specify the varying ratio of the order parameter, abbreviated as *VROP*. If $P_p$ is set as

35 the order parameter of a plain system, whereas $P_I$ is set as the order parameter of a system induced by confinements, then

$$VROP = \frac{(P_I - P_p)}{P_p}.$$

Based on this formula, a positive value of the parameter means the confinement acts as a reinforcing effect on phase

40 morphologies, i.e., it helps the system to form ordered mesoscale phases. On the contrary, a negative value means a weakening effect, i.e., it helps the system to form disordered mesoscale phases. Therefore, in Fig. 4, a reference line with *VROP* values of 0 is set as a boundary of the reinforcing and weakening effect.

45 Obviously, all of the confinements exert a reinforcing effect on A142, A121, A122 and B411, whereas they exert a weakening effect on B211; however, for other BCPs, there is no distinct pattern to follow. The mesoscale structures of twelve BCPs induced by wall confinements are displayed in Fig. 4; we found

50 no change in phase morphologies, except that B211 and B212 changed into cylindrical phases.
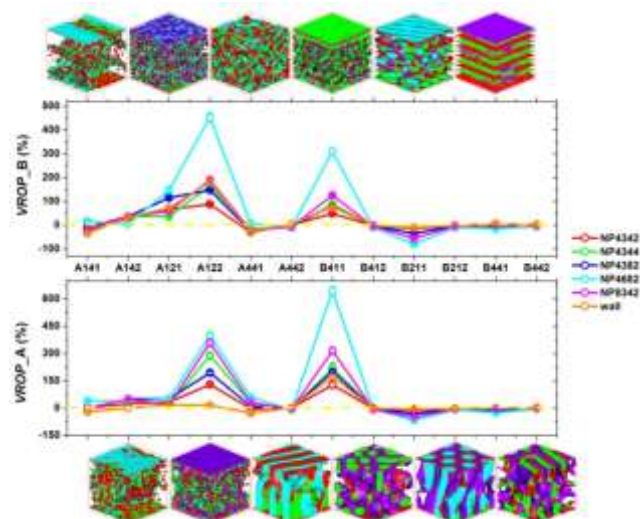


**Fig. 4**. *VROP* of twelve PEO-*b*-PMMA BCPs induced by various NPs and wall confinements. The reference line colored in yellow is the value

55 of 0. The mesoscale structures of short-chained BCPs restricted by neutral wall confinement are listed on the top, whereas the long-chained BCPs restricted by neutral wall confinement are listed at the bottom.
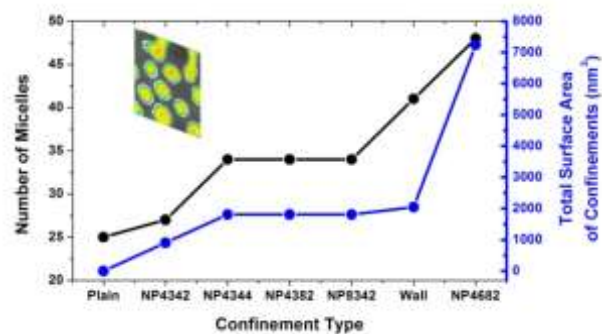


**Fig. 5**. Number of micelles of B412 BCP under various confinements. In

60 addition, the statistics of the total surface area of the corresponding confinements are displayed. The inserted picture is a representative density slice induced by NP4342.
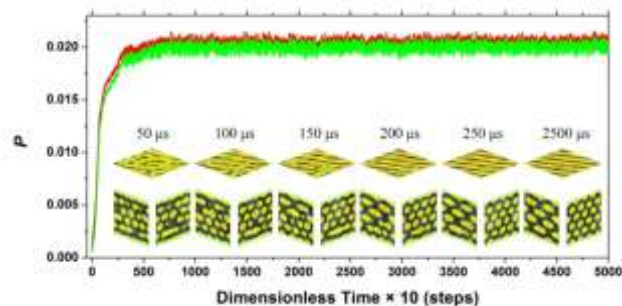


**Fig. 6**. Time evolution of the *P* values of the B211 BCP under the

65 "Wall55" confinement. The red line denotes the *P* values for A beads, whereas the green line denotes the *P* values for B beads. The inserted pictures are the density slices from one top view and two side views at a certain time. The spectrum of A density is in "White-Black" color mapping, whereas the spectrum of B density is in "Reverse Rainbow"

70 color mapping.

## Analysis of the phase morphology of B412 BCP

The mesoscale structures of B412 BCP are fixed, regardless of being in the form of ordinary BCP or under various

confinements, i.e., the B412 BCP self-assembled into a micelle phase with a core-shell structure, with most of them being spherical, as shown in the inserted picture Fig. 5, where the dense core consists of MMA segments, and the EO segments compose
5 the shell. Surprisingly, due to the excluded volume effect from confinement, a blank area is formed between the core and the shell, with the density of both A and B being nearly zero, resulting in a vesicle-like structure, which has many applications. Regardless of 2D confinement as a wall or 3D confinement as a
10 NP, the interaction between the surface of confinement and the polymeric species is the main driving force in such systems. Assuming that the surface density of confinement is uniform, an analysis of the total surface area of the six types of confinements was performed, with the results shown in Fig. 5. Regardless of
15 the shape, the order of the surface areas of the BCPs is NP4342 < NP4344 = NP4382 = NP8342 < Wall < NP4682, consistent with the same trend of the number of micelles under the corresponding confinement. With the introduction of confinement, the number of micelles is greater than that of the plain BCP, which
20 demonstrates the inducing effect of confinement on the refinement and uniformity of micelle shape and distribution and suggests a novel method to improve the properties of BCPs.

### The mechanism of the phase formation of B211 BCP under neutral and non-neutral wall confinement

25 The asymmetry in chain flexibility would lead to an effective wetting of surfaces by the more flexible species [37-38]. Owing to the limitation of MesoDyn methods, the discussion of the phase morphologies induced by the wall in this work is based on no difference in the flexibility of the PEO and PMMA blocks.
30 The neutral walls with non-preferential wetting of one of the polymeric species, whose interactions with both A and B beads, $\varepsilon_{Wall-A}$ and $\varepsilon_{Wall-B}$, respectively, are the same, i.e., 5.0 kJ • mol$^{-1}$; such neutral wall confinement is called "Wall55". In Fig. 6, the evolution of the phase formation is observed via the density slices
35 of both the A and B beads. Combined with the time evolution of the $P$ values and the density slices, apparently, there are four stages to describe the phase formation process, longitudinal stratification (Stage I), transverse orientation (Stage II), stripping (Stage III) and refinement (Stage IV). At Stage I, the initial
40 messy morphology turns into four stacked layers, aligned parallel to the wall, and another two slabs near the top and the bottom of the walls. The orientation of the aggregates in each layer is anisotropic; however, there are bulging parts with dense B density in these aggregates. The number of the layers remains
45 unchanged at Stage II; several bulging parts are distributed in cylinder-like aggregates, resulting in the high density of B beads. A general orientation trend of the aggregates is clear in 2,000 steps. However, some combination of two aggregates can still be observed from the side view. From 3,000 steps to 4,000 steps, the
50 decrease of the volume of the combined aggregates indicates the stripping process of the bulky aggregates into smaller ones, which characterizes Stage III. The period of Stage IV is from 4,000 steps to 5,000 steps, which involves a refinement process of the orientation of each column. Finally, the parallel four layers of
55 cylinders are formed, with uniform size and in hexagonal arrangement, including two layers of half-size of cylinder arrays, after 5,000 steps.
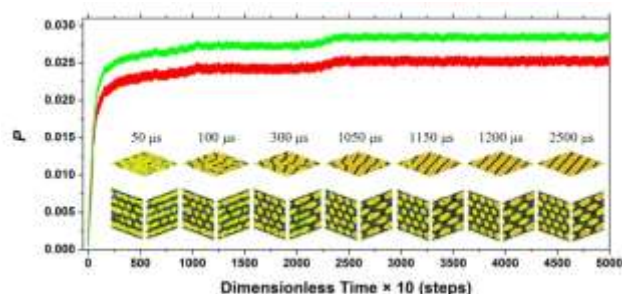


**Fig. 7**. Time evolution of the $P$ values of the B211 BCP under the
60 "Wall38" confinement. The red line denotes the $P$ values for A beads, whereas the green line denotes the $P$ values for B beads. The inserted pictures are the density slices from one top view and two side views at a certain time. The spectrum of A density is in "White-Black" color mapping, whereas the spectrum of B density is in "Reverse Rainbow"
65 color mapping.
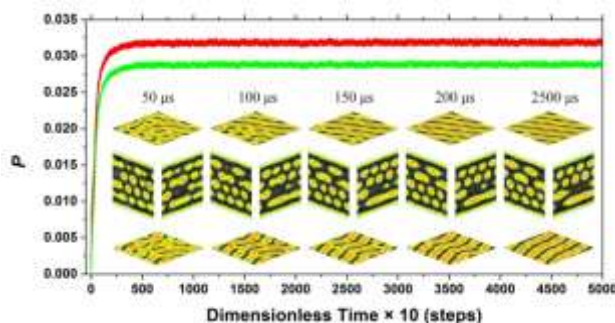


**Fig. 8**. Time evolution of the $P$ values of the B211 BCP under the "Wall83" confinement. The red line denotes the $P$ values for A beads, whereas the green line denotes the $P$ values for B beads. The inserted
70 pictures are the density slices from two top views (upper part and lower part) and two side views at a certain time. The spectrum of A density is in "White-Black" color mapping, whereas the spectrum of B density is in "Reverse Rainbow" color mapping.
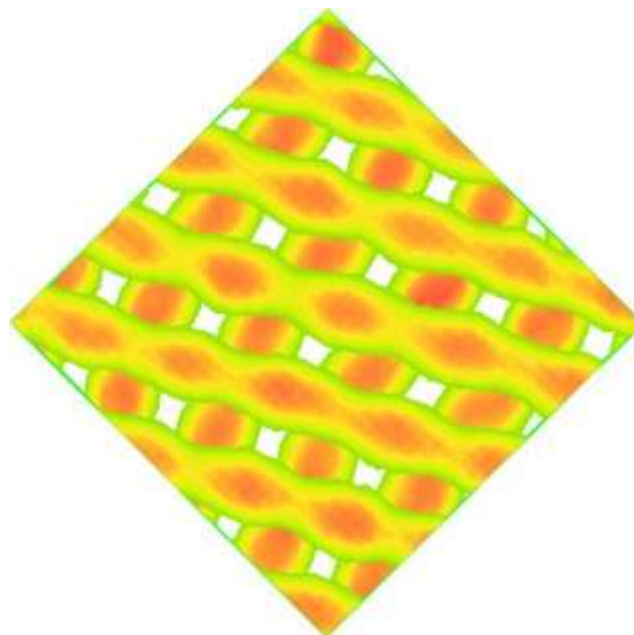


75 **Fig. 9**. The overlap of the density slices from both the upper and lower parts of B211 BCP under the "Wall83" confinement from the top view. The spectrum of B density is in "Reverse Rainbow" color mapping. For clarity, the density of A beads is omitted.

Because of the hydrophilic property of EO segments and the hydrophobic property of MMA segments, a non-neutral wall can be introduced. First, the wall has smaller repulsion with A beads than with B beads; their interaction pairs are $\varepsilon_{Wall-A} = 3.66$ and
[5] $\varepsilon_{Wall-B} = 8.88$, respectively, and this non-neutral wall confinement is called "Wall38". In Fig. 7, we also found four stages during the phase forming process, which is the same as the stages of Wall55, but the phase formation time is much longer, 24,000 steps, due to the time-consuming process in the Stage III, i.e., it takes the
[10] period from 2,000 steps to 23,000 steps (21,000 steps) to strip the budded cylinders into independent ones. With the absence of bulging parts in each cylinder, the B beads are distributed evenly. Notably, the acute angle of the orientation of the cylinder arrays to the horizon in top view is 69.3 degrees, which is greater than
[15] that of Wall55 of 17.6 degrees. This difference is the result of the competition between the interaction pair of wall-A and wall-B; thus, the orientation of the cylinder arrays changes significantly. However, there are no slabs formed near the walls; instead, one or more layers in the columnar phase are generated, and the
[20] cylinder arrays are also in a hexagonal arrangement.

Second, compared to Wall38, we converted the interactions between confinement and polymeric species and set the wall with greater repulsion with A beads but smaller repulsion with B beads; their interaction pairs are $\varepsilon_{Wall-A} = 8.88$ and $\varepsilon_{Wall-B} = 3.66$,
[25] respectively, and we refer to this non-neutral wall confinement as "Wall83". In Fig. 8, from the time evolution of the $P$ values, both the time and process of phase formation under Wall83 are quite similar to those of Wall55, but are different from those of Wall38, despite both Wall83 and Wall38 being non-neutral walls.
[30] Although the phase morphology also forms as columnar phase, surprisingly, there are two sets of columnar phases with different orientations, whose acute angle of the cylinder array to the horizon in top view is 18.3 degrees for the upper arrays and 56.7 degrees for the lower arrays, which is 0.7 degree greater than that
[35] of Wall55 and 12.6 degrees smaller than that of Wall38, respectively. Such a crossed columnar phase appears as mixed mesoscale structures, i.e., the equilibrium structure is a copy of Wall55 as its upper part and a duplicate of Wall38 as its lower part. However, the refinement stage for the lower part is a time-
[40] consuming process, lasting for nearly the entire simulation time to refine the curved cylinder arrays. In addition, there are two slabs formed near the top and bottom walls; thus, only four layers of the columnar phase finally formed. The bulging parts can also be found in the cylinder tubes with dense B cores in both the
[45] upper and lower parts, which are formed by the stack of the cylinder arrays. The bulging parts on the upper layer exist in the intermediate section of the adjacent cylinder arrays on the lower layer, and vice versa, as shown in Fig. 9. The intersection angle between the upper and lower cylinder arrays is 75.0 degrees.
[50] Certainly, the formation of these sets of cylinder arrays under non-neutral walls confinement is also the result of the difference in the interaction between wall-A and wall-B. However, from an analysis of the short phase formation time, approximately 4,000 steps, with the mesoscale structures cooperating, it is clear that
[55] the forming processes in both upper and lower parts are synchronous. Notably, two slabs are formed simultaneously on the top and at the bottom of this system; thus, they act as a barrier between the wall confinement and the polymeric system between

two slabs, resulting in the weakening of the wall-A and wall-B
[60] interactions. From a thermodynamic perspective, such a crossed columnar phase is the most stable phase.
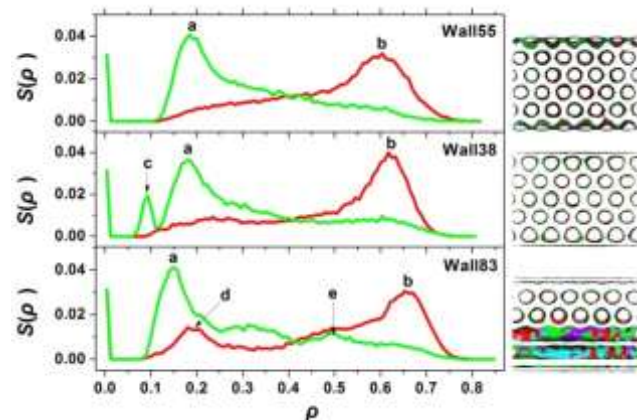


**Fig. 10**. The density distribution of the B211 BCP under "Wall55", "Wall38" and "Wall83" confinements. The red line denotes the density of
[65] A beads, whereas the green line denotes the density of B beads. The inserted pictures are the corresponding mesoscale structures along the axial direction of cylinder arrays. Red represents the isosurface of A beads, and purple represents the isosurface of A'; green represents the isosurface of B beads, and cyan represents the isosurface of B'.
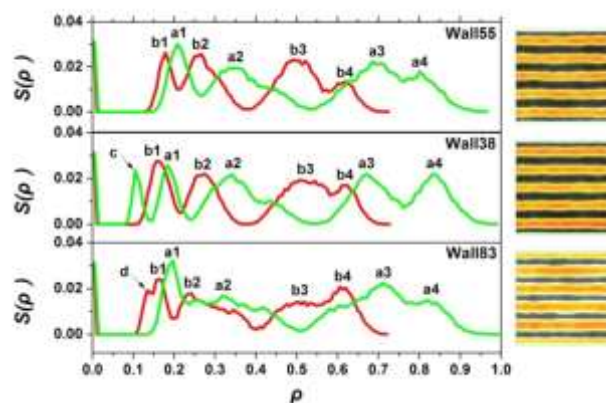


[70]
**Fig. 11**. The density distribution of the B441 BCP under "Wall55", "Wall38" and "Wall83" confinements. The red line denotes the density of A beads, whereas the green line denotes the density of B beads. The inserted pictures are the corresponding density slices. The spectrum of A
[75] density is in "White-Black" color mapping, whereas the spectrum of B density is in "Reverse Rainbow" color mapping.

The statistics of the density distribution of B211 BCP under Wall55, Wall38 and Wall85 confinements are shown in Fig. 10. Both peak a and peak b are common in these three density
[80] distributions, which indicates the core-shell mesoscale structure. Peak c reveals the additional B beads assembled at the bottom of the cylinder arrays nearest the walls. However, except for the pair of peaks a and b, the additional pair of peaks d and e certify the existence of another type of cylinder array being formed. More
[85] information can be obtained from the mesoscale structures shown on the right side of Fig. 9: all of these cylinder arrays are arranged in the columnar phase. In such a $32 \times 32 \times 32$ nm$^3$ box, six cylinders are generated in one row of these three walls. However, for Wall55, four rows of entire cylinder array and two
[90] more partial cylinder arrays form near the walls; for Wall38, five

rows of entire cylinder arrays are generated, and no defect appears; for Wall83, four rows of entire cylinder arrays are found, but the top two and the lower two are of different orientations; in addition, two slabs are formed near the walls. These differences are generated from the interaction between polymeric species and the wall. When there is no preference, e.g., Wall55, both A beads and B beads have the same probability of adsorbing near the walls; in this case, the mesoscale structure primarily depends on the molecular topology of BCP. Therefore, the mesoscale structures near the walls also adopt a core-shell structured columnar phase, but the space limits it to form a perfect cylinder, only in halves. When the interaction of A beads to the wall is smaller than that of B, e.g., Wall38, A beads have a greater probability of gathering near the wall, whereas B beads are repelled away from the wall; thus, several B beads gather outside of the nearest cylinder arrays to the walls, so the radius of these cylinder arrays is slightly greater than that of the inside cylinder arrays. However, when the wall prefers the adsorption of B beads, e.g., Wall83, the repulsion of the wall to A beads compels two slabs to be produced, which is one of the primary reasons for the formation of the crossed columnar phases.

### An analysis of the mesoscale structure of B441 under wall confinement

In Fig. 11, the density distribution of both A and B beads, both exhibiting the periodic variation, indicates the presence of a periodic structure, as shown in the mesoscale structures. Regardless of the type of wall confinement, there are four obvious peaks of both A (peak b1, b2, b3 and b4) density and B density (peak a1, a2, a3 and a4) in common, and the lack of overlap of any peaks indicates that all the arms are in stretch configurations with no entanglement between A and B segments. In addition, when the wall confinement changes from neutral to non-neutral, a new peak appears, e.g., peak c of B beads (with the most repulsive parameter) in Wall38 and peak d of A beads (with the most repulsive parameter) in Wall83. Both of these new-born peaks reflect the unbalanced interaction of the wall to the A and B beads, i.e., the beads that suffer a greater repulsive effect from wall confinement would form new aggregates that are slightly different from the mesoscale structure under a neutral wall. In particular, there is a vacant gap of both A and B densities between two interval slabs; this gap results from the preferred adsorption of B beads with weaker repulsive effect onto the walls, resulting in the formation of B slabs near walls, which weaken the interaction of the wall to the polymeric species.

## Conclusions

In the quantum calculations describing the homopolymers PEO and PMMA, the electrostatic properties were introduced as a Donnan effect into MesoDyn models, which satisfied the imitation of polyelectrolyte. To mimic the lipid structure, we designed twelve PEO-*b*-PMMA BCPs in miktoarm structures with various molecular topologies, short or long chain or of different arm numbers. The self-assembly of weak polyelectrolyte PEO-*b*-PMMA BCPs under the doping effect of nanoparticles was investigated with the aid of MesoDyn simulations, with the following phases considered: disordered (A141, A142, A121, A122, A441 and B411), curved lamellar (A442 and B442),

micelles (B412, B211 and B212), and lamellar (B441) phases. Compared to short-chained BCPs, the long-chained BCPs present more ordered phase morphologies. Furthermore, macrophase separation occurs in A442, B412, B212 and B442 BCPs, due to their *P* values being higher than 0.1. A142, A121, A122 and B411 experience the reinforcing effect from all forms of confinements, whereas B211 exhibits a weakening effect of the confinement.

We concentrated on B412 because of its core-shell structured micelles phase under different situations, in particular, the portion of B412 near the 2D or 3D confinements, an ultra-dilute density of polymeric species formed between the core and shell, which is in vesicle-like structure due to the excluded volume effect of confinement. With the same interaction between confinement and polymeric species, we found that the generated micelle number increases in proportion with the increase of the total surface area of NPs and the wall confinements. This result confirmed that the function of confinement can be a method to regulate the properties of materials.

The two hydrophilic EO segments and one hydrophobic MMA segment in B211 BCP enable self-assembly from the micellar phase to columnar phase under wall confinements, with the cylinder arrays being in a hexagonal arrangement. We found four stages (i.e., longitudinal stratification, transverse orientation, stripping and refinement) during the phase formation. The time periods of phase formation under Wall55 and Wall83 are 5,000 steps and 4,000 steps, respectively, which are much shorter than that of Wall 38 of 24,000 steps. The cylinder arrays have bulging parts distributed evenly along the axial direction with dense cores of B beads under both Wall55 and Wall83 confinements, but there are no bulging parts formed under Wall38 confinement. The primary reason for this behavior is the difference in the interaction between wall and polymeric species. Interestingly, such interaction can form a crossed columnar phase under non-neutral wall confinement, with the greater repulsive effect of the wall to hydrophilic segments, and the intersection angle of these two sets cylinder arrays is 75.0 degrees. The behavior serves as a promising reference for the manufacturing of nano-columnar tube arrays with different orientation, which can be applied in electronics, material processing, and other industries.

The introduction of neutral and non-neutral wall confinement into B441 BCP was also investigated briefly. The reason for the formation of the lamellar phase with an interval arrangement of EO and MMA segments is its special molecular topology, for which a symmetrical distribution of these four arms, consisting of both EO and MMA segments, is found. When the wall to A beads results in preferential repulsive interaction, a vacant gap between two interval slabs is formed, which provides a novel method to strip various lamels in a manner similar to desorption.

## Acknowledgments

## Notes and references

[a] *Institute of Research on the Structure and Property of Matter, Zaozhuang University, Zaozhuang, 277160, China. E-mail: mudanjlu1980@163.com*

[b] *Opto-Electronic Engineering College, Zaozhuang University, Shandong 277160, China. E-mail: lijq786@163.com*

[c] *School of Chemistry and Chemical Engineering, Shandong University, Jinan, 250100, China; E-mail: fsy@sdu.edu.cn*

5

1　C. Giacomelli, V. Schmidt and R. Borsali, *Macromolecules*, 2007, **40**, 2148.

2　M. Rubinstein and R. H. Colby, *Polymer Physics*, Oxford University Press: Oxford, UK, 2003.

10　3　S. Thomas, D. Durand, C. Chassenieux and P. Jyotishkumar, *Handbook of Biopolymer-Based Materials: From Blends and Composites to Gels and Complex Networks*, John Wiley & Sons, 2013.

4　F. Oosawa, *Polyelectrolytes*, Marcel Dekker, New York, 1971.

15　5　A.V. Kyrylyuk and J.G.E.M. Fraaije, *J. Chem. Phys.*, 2004, **121**, 2806.

6　N.S. Cameron, A. Eisenberg and G.R. Brown, *Biomacromolecules*, 2002, **3**, 124.

7　S. Förster, N. Hermsdorf, W. Leube, H. Schnablegger, M. Regenbrecht, S. Akari, P. Lindman and C. Böttcher, *J. Phys. Chem. B*, 1999, **103**, 6657.

8　M. Regenbrecht, S. Akari, S. Förster and H. Möhwald, *J. Phys. Chem. B*, 1999, **103**, 6669.

9　J.L. Barrat and J.F. Joanny, *Adv. Chem. Phys.*, 1996, **XCIV**.

25　10　C. Holm, J.F. Joanny, K. Kremer, R.R. Netz, P. Reineker, C. Seidel, T.A. Vilgis and R.G. Winkler, *Adv. Polym. Sci.*, 2004, **166**, 67.

11　S. Förster and M. Schmidt, *Physical Properties of Polymers*, Springer, 1995.

12　V.Y. Borue and I.Y. Erukhimovich, *Macromolecules*, 1988, **21**, 3240.

13　A.N. Kudlay, I.Y. Erukhimovich and A.R. Khokhlov, *Macromolecules*, 2000, **33(15)**, 5644.

14　M. Castelnovo and J.F. Joanny, *Macromolecules*, 2002, **35(11)**, 4531.

35　15　A.V. Dobrynin, *Macromolecules*, **2006**, 39, 9519.

16　N.P. Shusharina, E.B. Zhulina, A.V. Dobrynin and M. Rubinstein, *Macromolecules*, 2005, **38(21)**, 8870.

17　Q. Liao, A.V. Dobrynin and M. Rubinstein, *Macromolecules*, 2006, **39**, 1920.

40　18　J.G.E.M. Fraaije, B.A.C. van Vimmeren, N.M. Maurits, M. Postma, O.A. Evers, C. Hoffmann, P. Altevogt and G. Goldbeck-Wook, *J. Chem. Phys.*, 1997, **106**, 4260.

19　B.A.C. van Vlimmeren, N.M. Maurits, A.V. Zvelindovsky, G.J.A. Sevink and J.G.E.M. Fraaije, *Macromolecules*, 1999, **32**, 646.

45　20　Y.M. Lam and G. Goldbeck-Wook, *Polymer*, 2003, **44**, 3593.

21　E. Huang, T.P. Russell, C. Harrison, P.M. Chaikin, R.A. Register, C.J. Hawker and J. Mays, *Macromolecules*, 1998, **31(22)**, 7641.

22　G.T. Pickett and A.C. Balazs, *Macromolecules*, 1997, **30(10)**, 3097.

23　Y.M. Huang, H.L. Liu and Y. Hu, *Macromol. Theory Simul.*, 2006, **15**, 117.

24　Y.M. Huang, H. Xia, H.L. Liu and Y. Hu, *Macromol. Theory Simul.*, 2007, **16(1)**, 93.

25　X.Q. Xiao, Y.M. Huang, H.L. Liu and Y. Hu, *Macromol. Theory Simul.*, 2007, **16**, 732.

55　26　J. Feng and H.L. Liu, *Fluid Phase Equilib.*, 2007, **261**, 50.

27　J. Feng, H.L., Liu, Y. Hu and J.W. Jiang, *Macromol. Theory Simul.*, 2008, **17**, 163.

28　D. Mu, J.Q. Li and S.Y. Feng, *Polym. Int.*, 2014, **63(3)**, 568.

29　D. Mu, X.R. Huang, Z.Y. Lu and C. C. Sun, *Chem. Phys.*, 2008, **348**, 122.

30　J. Crank and P. Nicolson, *Proc. Camb. Phil. Soc.*, 1947, **43**, 50.

31　S.L. Yuan, X.Q. Zhang, G.Y. Xu and D.J Zhang, *J. Mol. Model.*, 2006, **12**, 406.

32　A.V. Kyrylyuk and J.G.E.M. Fraaije, J. Chem. Phys., 2004, 121(18), 9166.

33　S.R. de Groot and P. Mazur, *Non-Equilibrium Thermodynamics*, Dover Publications: New York, 1983.

34　J. Fraaije, B. Van Vlimmeren, N. Maurits, M. Postma, O. Evers, C. Hoffmann, P. Altevogt and G. Goldbeck-Wood, *J. Chem. Phys.*, 1997, **106**, 4260.

70

35　P. Altevogt, O.A. Evers, J.G.E.M. Fraaije, N.M. Maurits and B.A.C. van Vlimmeren, *J. Mol. Struc-Theochem.*, 1999, **463**, 139.

36　S.S. Jawalkar and T.M. Aminabhavi, *Polymer*, 2006, **47(23)**, 8061.

37　D.T. Wu, G.H. Fredrickson and J.P. Carton, *J. Chem. Phys.*, 1996, **104(16)**, 6387.

75

38　A. Nikoubashman, R.A. Register and A.Z. Panagiotopoulos, *Macromolecules*, 2014, **47**, 1193.

**Soft Matter Accepted Manuscript**